Engineering Structures 200 (2019) 109701

Contents lists available at ScienceDirect

Engineering Structures

journal homepage: www.elsevier.com/locate/engstruct

Progressive collapse simulation of the steel-concrete composite floor system considering ductile fracture of steel

Junjie Wang[a,b], Wei Wang[a,b,*], Xudong Qian[c]

[a] State Key Laboratory of Disaster Reduction in Civil Engineering, Tongji University, Shanghai 200092, China
[b] Department of Structural Engineering, Tongji University, Shanghai 200092, China
[c] Department of Civil and Environmental Engineering, Centre for Offshore Research and Engineering, National University of Singapore, Singapore 117576, Singapore

ARTICLE INFO

Keywords:
Ductile fracture
Lode angle
Stress triaxiality
Progressive collapse
Steel moment frame

ABSTRACT

The prediction of the structural behavior under the progressive collapse scenario has received growing attentions in recent years. The failure of the bolted shear tab connection is usually dominated by the shear fracture. However, few researchers have considered the effect of the shear fracture in the progressive collapse simulation. This research develops a practical modeling routine to upscale the material shear fracture model in the collapse simulation of a large-scale floor system. The calibration and validation of the material shear fracture model employ five types of plate coupon specimens with significantly different stress triaxiality and Lode angle parameters. Via optimizing the coupon test data, this study determines the 3-D fracture locus of three fracture models, which are subsequently used to predict the fracture of a coupon specimen in the tension and shear conditions. Among the three fracture models, the Bai model has demonstrated good accuracy for a wide range of stress triaxiality and Lode angle parameters, while the applicability of the other two fracture models are confined to the stress triaxiality and Lode angle parameters, from which they are calibrated. These fracture models are also used to simulate the fracture of a girder-to-column connection under a center column removal scenario, which indicates the fracture in both the girder flange and girder web depends highly on the Lode angle. Prior to analyzing the full-scale composite floor system, the numerical study calibrates the fracture strain in the macro shell elements used to build the girder-to-column connection model, based on the fracture locus determined from the coupon tests. The fracture strain based shell element model is then used in the steel-concrete composite floor simulation, and demonstrates a good prediction of the structural resistance curve and the failure mode compared to the experimental results.

1. Introduction

Progressive collapse of structures often originates from local failures, which are often triggered by natural or artificial disasters, and propagate to the critical components, and subsequently to the entire structure [1]. The ductile fracture represents a primary failure mechanism in well-designed and constructed steel structures during the progressive collapse [2], especially in the beam-to-column connections. Furthermore, the failure of the bolted connection is likely to be dominated by the shear fracture [3], which depends on the Lode angle.

In recent decades, the shear fracture governed by the Lode angle were comprehensively investigated by several reseachers. Through fracture test of metallic materials over a wide range of stress triaxialities, Bao and Wierzbicki [4,5] found that the fracture locus does not necessarily follow a smooth, monotonic curve in the entire range of stress triaxiality caused by the correspondingly different fracture mechanisms. In the range of high stress triaxialities, the steel fracture mechanism follows the void growth model, while at low stress triaxialities, fracture may develop as a combination of shear and void growth modes. Wilkins [6] was the first to introduce the effect of Lode angle θ, which is related to the third deviatoric stress invariant and is often neglected in the ductile fracture models. In Wilkins′ model, the stress triaxiality and Lode angle are separable. Besides, the fracture locus is symmetric with respect to the Lode angle. Xue [7] extended Wilkins′ model into a non-separable but symmetric 3D fracture locus in the space of stress triaxiality and the normalized third stress invariant. Recently, Bai [8] has proposed a general asymmetric fracture locus in the 3D space of equivalent plastic fracture strain ε_f, stress triaxiality η, and the Lode angle parameter. The asymmetric fracture locus consists of six parameters, but reduces to four parameters if the fracture locus

* Corresponding author at: State Key Laboratory of Disaster Reduction in Civil Engineering, Tongji University, Shanghai 200092, China.
E-mail address: weiwang@tongji.edu.cn (W. Wang).

https://doi.org/10.1016/j.engstruct.2019.109701
Received 12 June 2019; Received in revised form 15 September 2019; Accepted 19 September 2019
Available online 27 September 2019

Nomenclature

D_1, D_2, D_3, D_4, D_5, D_6, D_0	fracture parameters for fracture models
f_t	maximum tensile strength of concrete
G_f	fracture energy of concrete
l_c	element size
T	temperature
Δ_u	crack opening displacement of concrete
ε	true strain
ε_f	plastic fracture strain
ε_{nom}	nominal strain
ε_f^+	bounding curve corresponding to the axisymmetric tension
ε_f^0	bounding curve corresponding to the plane strain
ε_f^-	bounding curve corresponding to the axisymmetric compression
η	stress triaxiality
η_{avg}	average value of the stress triaxiality
θ	Lode angle
$\bar{\theta}$	Lode angle parameter
$\bar{\theta}_{avg}$	average value of the Lode angle parameter
ξ	Lode angle parameter
σ	true stress
σ_c	negative part of the effective stress tensor
σ_{eq}	effective stress
σ_m	mean stress
σ_{nom}	nominal stress
σ_t	positive part of the effective stress tensor
ω_c	compressive damage variable
ω_t	tensile damage variable

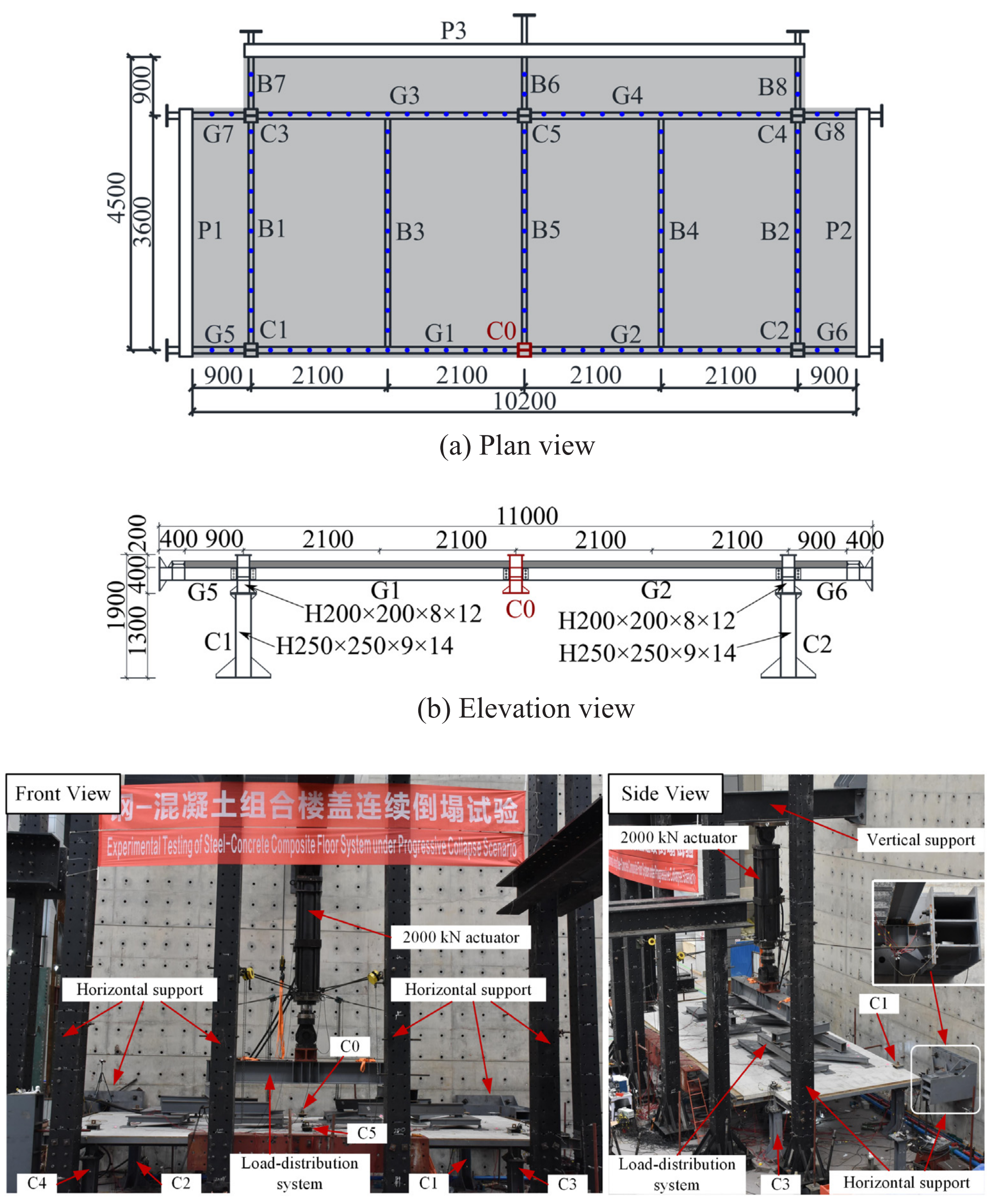

(a) Plan view

(b) Elevation view

(c) Test setup

Fig. 1. Specimen dimensions and test setup for the composite floor system.

assumes a symmetric shape with respect to the Lode angle. Bai [9] has demonstrated the accuracy of the four-parameter symmetric model for the steel fracture. Therefore, this study adopts the four-parameter Bai model with symmetric assumptions for the progressive collapse simulation.

Up to now, many researchers have reported nonlinear finite-element analyses of the progressive collapse behaviors of composite floor systems. These include work performed by Sadek [10], Alashker [11–13], Li [14], Main and Liu [15], Fu [16,17], Kwasniewski [18]. In these finite-element analyses, comprehensive parametric investigations on the failure modes had been conducted by altering structural configurations, material properties, loading schemes, etc. However, few of them have considered the Lode angle in the progressive collapse simulation.

The present paper develops a convenient calibration procedure of Bai model [9] for steel materials subjected to monotonic steel shear fracture, and proposes a simple method to incorporate this shear fracture effect in the structural level simulation. In addition to Bai model, this study also compares the fracture locus calibrated from the Rice-Tracey (RT) model and the Constant Fracture Strain (CFS) model. Among the three models, Bai's model has demonstrated enhanced accuracy when compared against the material coupon specimens subjected to shear and tension loads. Beyond the material level comparison, the numerical analysis of a rigid girder-to-column connection under tension and bending reveals clear dependence of the fracture failure on the Lode angle. To facilitate the engineering assessment of shear fracture in large scale structures, this study proposes an empirical conversion to consider the shear fracture effect in the girder-to-column connection using shell elements. Subsequently, the numerical investigation demonstrates the feasibility of using this modified shell element modeling method in simulating the progressive collapse of a composite floor system.

2. Composite floor system test

The experimental program in this study examines a 2 × 1 bay full-scale steel-concrete composite floor system under monotonically increasing quasi-static loading with a middle edge column removed to simulate the progressive collapse scenario. Fig. 1 shows the specimen details, where the symbols "C," "G," "B" and "P" represent columns, girders, beams, and peripheral beams, respectively. The span length of girders and beams are 4.2 m and 3.6 m, respectively. The column height is 1.8 m, which equals half of the storey height. The girder, beam, and column adopt standard sections [19] of H200 × 100 × 5.5 × 8, H150 × 75 × 7 × 10, and H200 × 200 × 8 × 12, respectively. "H200 × 100 × 5.5 × 8" represents an H-section beam, for which the beam height, flange width, flange thickness and web thickness are 200 mm, 100 mm, 8 mm, 5.5 mm, respectively. The connection between the steel beams and composite slab utilizes the 16 mm-diameter 80 mm-height shear studs with spacings of 300 mm along the girder axis and 305 mm along the beam axis. As shown in Fig. 1(c), the point load from the actuator was equally distributed to 24 loading points on the slab by a load-distribution system. The lateral movements of the extended girders, i.e., G5, G6, G7, G8, and the extended beams, i.e., B6, B7, B8, were constrained by the horizontal supports to simulate the boundary condition provided by neighboring structural members.

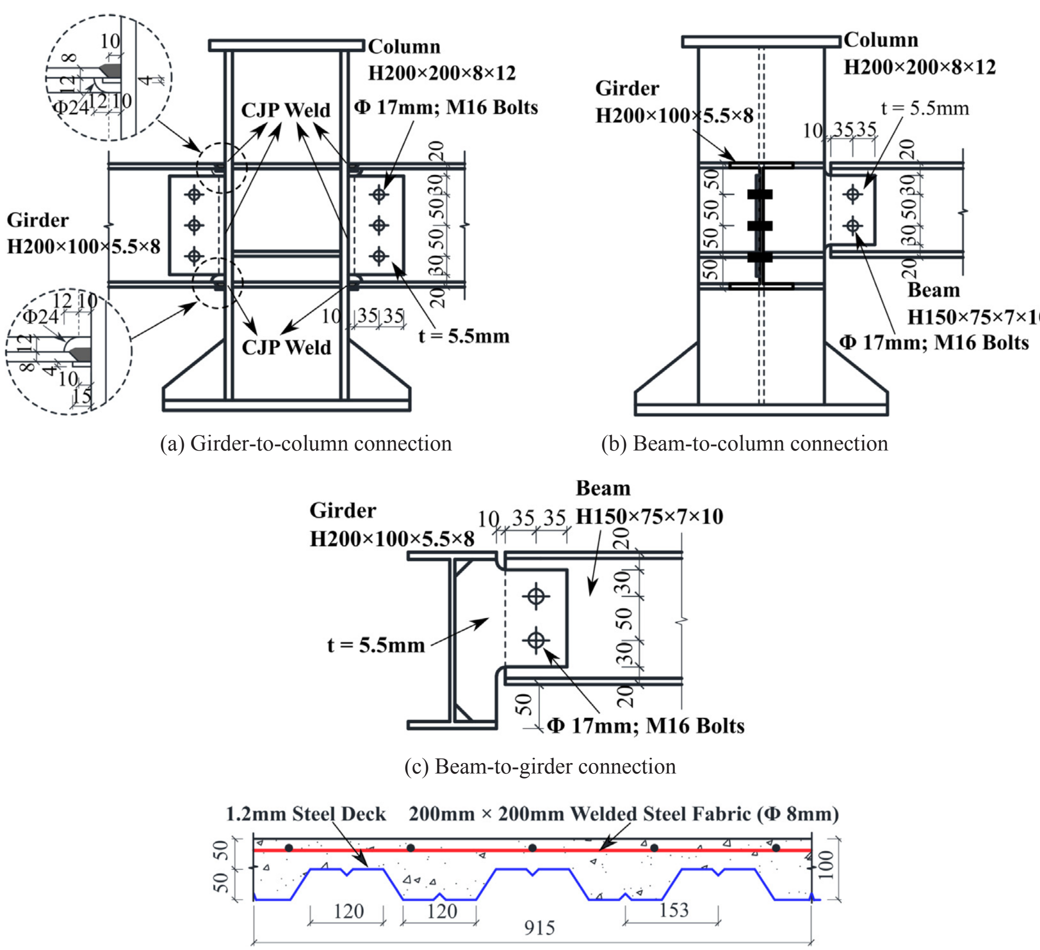

(a) Girder-to-column connection

(b) Beam-to-column connection

(c) Beam-to-girder connection

(d) Dimensions of the composite slab

Fig. 2. Connection details of the prototype structure.

Table 1
Mechanical properties of steel materials for different elements in various structural members.

Steel member	Location	Yield stress (MPa)	Ultimate stress (MPa)	Elongation (mm/mm)
Girder	Flange	390	536	0.31
	Web	419	557	0.31
Beam	Flange	365	517	0.31
	Web	400	535	0.32
Column	Flange	373	531	0.32
	Web	395	546	0.31
Rebar	Slab	596	672	0.07
Steel deck	Slab	320	380	0.38
Shear stud	Slab	320	400	0.14
Bolt	Connection	940	1040	0.10

As illustrated in Fig. 2, the girder-to-column connection employs the welded flange-bolted web moment resisting connection, while the beam-to-column and beam-to-girder connections are simple shear tab connections. The M16 (16 mm in nominal diameter) Grade 10.9 frictional high-strength bolts are employed to connect the girder/beam web with the extended shear tab. The shear tab is fabricated by the girder web. All high-strength bolts are applied with a pre-tension force of 100 kN. The thickness of the composite slab is 100 mm, and the thickness of the trapezoidal steel deck is 1.2 mm. The concrete slab contains a 200 × 200 mm CRB550 welded steel fabric with a clear cover of 15 mm. The diameter of the steel fabric is 8 mm.

Table 1 lists the mechanical properties of the structural steels, rebars, steel decks and the shear studs, all measured from coupon specimens, except for the shear studs and high-strength bolts, which adopt the nominal material properties provided by the manufacturers. The 28-day compressive strength of the concrete equals 33 MPa, measured from the 150 mm × 150 mm × 150 mm cubes on the same day as the floor test.

Fig. 3(a) presents the applied vertical load versus the vertical displacement measured below the slab at the position corresponding to the removed column (C0) for the tested specimen. Two important failure events occurred at the two distinctive peaks in the load-deformation curve: the fracture failure of the top flange of the G1-C1 connection [see Fig. 1(a) and 1(b)] followed by the failure of the residual section of the G1-C1 connection, as illustrated in Fig. 3(b), which shows the failure after the test. Cracking in the top flange of the G1-C1 connection triggers additional vertical displacement and initiates the transition from the flexural mode to the catenary-membrane mode, while the complete separation of the G1-C1 connection breaks the load path in the catenary action, leading to the peak resistance and a rapid deterioration in the post-peak resistance. Therefore, the crack extension in the girder-to-column connection determines directly the response of this composite floor in the progressive collapse test. The following section aims to integrate the material fracture response in simulating the fracture failure in the structural component as well as the global structure.

3. Fracture parameter calibration

The calibration of the fracture locus under high stress triaxiality often utilizes the round bar and notched round bars under uniaxial tension. Due to the limited thickness of the steel section in the floor test, fabrication of the notched round bars becomes practically challenging. This study, therefore, makes use of the plate specimens and holed plate specimens to replace the round bar and notched round bar specimens. This section presents the calibration procedure for the fracture locus using the thin plate specimens based on the simplified symmetrical Bai model.

3.1. Fracture model

In the six-parameter asymmetric model proposed by Bai [9] in Fig. 4(a), the fracture locus has three bounding curves, $\varepsilon_f^+ = D_1 e^{-D_2\eta}$ (corresponding to the axisymmetric tension, $\bar{\theta} = 1$), $\varepsilon_f^0 = D_3 e^{-D_4\eta}$ (corresponding to the plane strain or generalized shear loading condition, $\bar{\theta} = 0$), and $\varepsilon_f^- = D_5 e^{-D_6\eta}$ (corresponding to the axisymmetric compression, $\bar{\theta} = -1$). Eq. (1) defines this asymmetric model, which has six parameters, D1, D2, D3, D4, D5, and D6 to be calibrated.

$$\begin{aligned}\varepsilon_f(\eta,\bar{\theta}) &= \left[\frac{1}{2}(\varepsilon_f^+ + \varepsilon_f^-) - \varepsilon_f^0\right]\bar{\theta}^2 + \frac{1}{2}(\varepsilon_f^+ - \varepsilon_f^-)\bar{\theta} + \varepsilon_f^0 \\ &= \left[\frac{1}{2}(D_1 e^{-D_2\eta} + D_5 e^{-D_6\eta}) - D_3 e^{-D_4\eta}\right]\bar{\theta}^2 \\ &\quad + \frac{1}{2}(D_1 e^{-D_2\eta} - D_5 e^{-D_6\eta})\bar{\theta} + D_3 e^{-D_4\eta}\end{aligned} \tag{1}$$

where η denotes the stress triaxiality and $\bar{\theta}$ refers to the Lode angle parameter. The range of $\bar{\theta}$ is $[-1,1]$.

$$\eta = \frac{\sigma_m}{\sigma_{eq}} \tag{2}$$

$$\sigma_m = \frac{1}{3}(\sigma_1 + \sigma_2 + \sigma_3) \tag{3}$$

$$\sigma_{eq} = \sqrt{\frac{1}{2}[(\sigma_1 - \sigma_2)^2 + (\sigma_2 - \sigma_3)^2 + (\sigma_1 - \sigma_3)^2]} \tag{4}$$

$$\bar{\theta} = 1 - \frac{2}{\pi}\arccos\xi \tag{5}$$

$$\xi = \frac{27 s_1 s_3 s_3}{2\sigma_{eq}^3} = \cos(3\theta) \tag{6}$$

where (σ_1, σ_2, σ_3) are the three principal stresses, while (s_1, s_2, s_3) represent the three principal deviatoric stresses. σ_{eq} corresponds to the

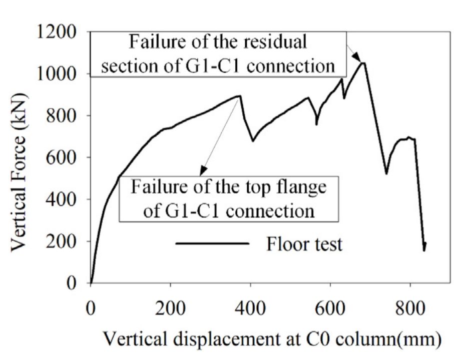

(a) Load-displacement curve

(b) Failure of the G1-C1 connection

Fig. 3. Failure modes of the experimental test.

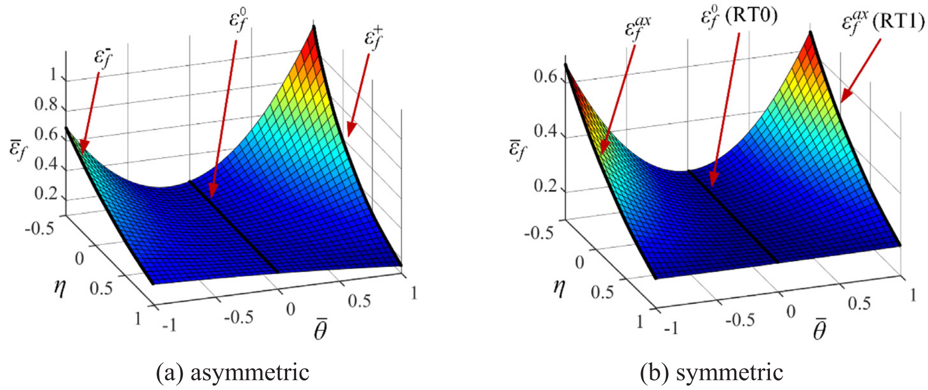

Fig. 4. 3D fracture locus.

Table 2
Summary of the coupon test specimen.

Type of Specimens	Specimen Name	η	$\bar{\theta}$
No. 1	Plate specimen	≈0.33	≈1
No. 2	Hole Plate specimen	> 0.33	≈1
No. 3	Notched Plate Specimen	> 1/√3	≈0
No. 4	90° Shear Plate Specimen	≈0	≈0
No. 5	45° Shear Plate Specimen	> 0	$0 < \bar{\theta} < 1$

mises effective stress, and σ_m is the mean stress. θ stands for the Lode angle, which ranges over $0 \le \theta \le \pi/3$. ξ is another Lode angle parameter.

If the symmetric fracture locus is assumed, as proposed by a number of researchers [7,20,21], the bounding curves ε_f^+ becomes identical to ε_f^-, as demonstrated in Fig. 4(b). The middle term in Eq. (1) thus vanishes, which implies that the damage evolution depends only on the absolute magnitude of the Lode angle parameter $\bar{\theta}$. Assuming $\varepsilon_f^+ = \varepsilon_f^- = \varepsilon_f^{ax}$, Fig. 4(b) illustrates the four-parameter symmetric Bai model. Eq. (7) defines this symmetric Bai model, which has four parameters, D1, D2, D3, D4, to be determined,

$$\varepsilon_f(\eta, \bar{\theta}) = [\varepsilon_f^{ax} - \varepsilon_f^0]\bar{\theta}^2 + \varepsilon_f^0 = [D_1 e^{-D_2\eta} - D_3 e^{-D_4\eta}]\bar{\theta}^2 + D_3 e^{-D_4\eta} \quad (7)$$

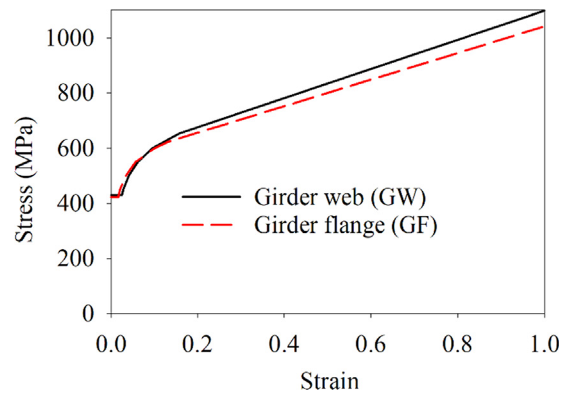

Fig. 6. The true stress-strain relationship.

At least four distinct sets of (ε_f, η, $\bar{\theta}$) measured from the steel coupon test are necessary to calibrate the symmetric Bai model.

In addition to the Bai model, the following section also calibrates the Rice-Tracey model [22], namely the RT model. As shown in Eq. (8), the Bai model reduces to the RT model when the Lode angle parameter $\bar{\theta}$ is zero,

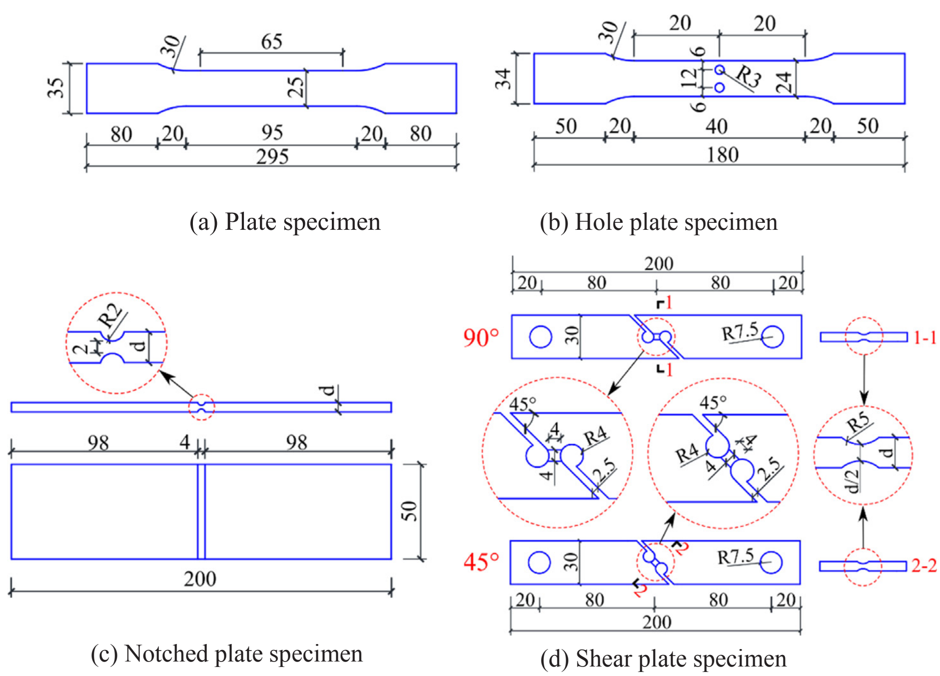

Fig. 5. Coupon test specimen details.

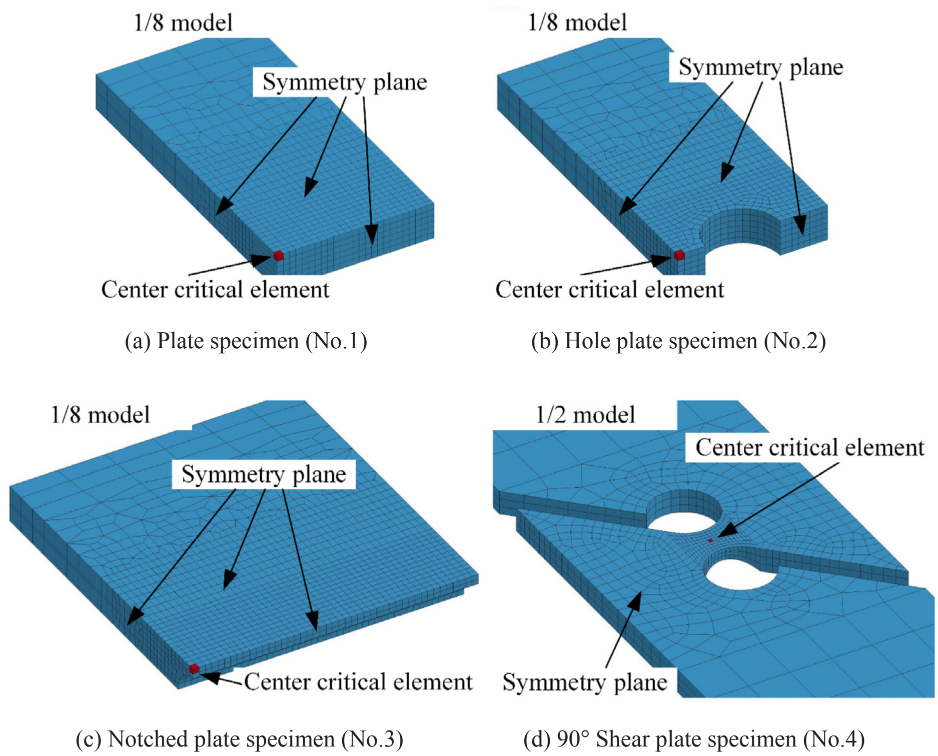

Fig. 7. Elements (shown in red) analyzed for triaxiality and Lode angle parameter for each specimen. (For interpretation of the references to colour in this figure legend, the reader is referred to the web version of this article.)

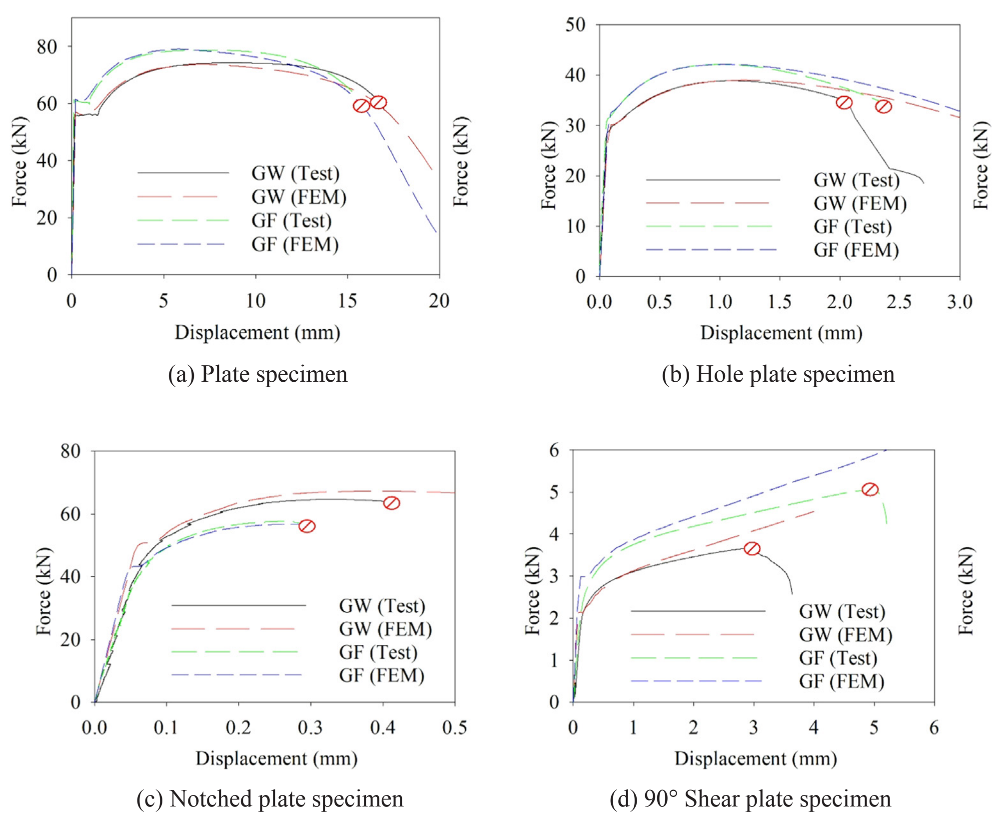

Fig. 8. Force-displacement curve of each specimen.

$$\varepsilon_f(\eta) = \varepsilon_f^0 = D_3 e^{-D_4\eta} \tag{8}$$

The bounding curves ε_f^{ax} and ε_f^0 in Fig. 4(b), denoted as RT1 and RT0, represent the RT models at $\bar{\theta} = 1$ and $\bar{\theta} = 0$, respectively. By further setting the stress triaxiality to zero, Eq. (8) becomes a simple "Constant Fracture Strain (CFS) model".

$$\varepsilon_f = D_0(\text{constant}) \tag{9}$$

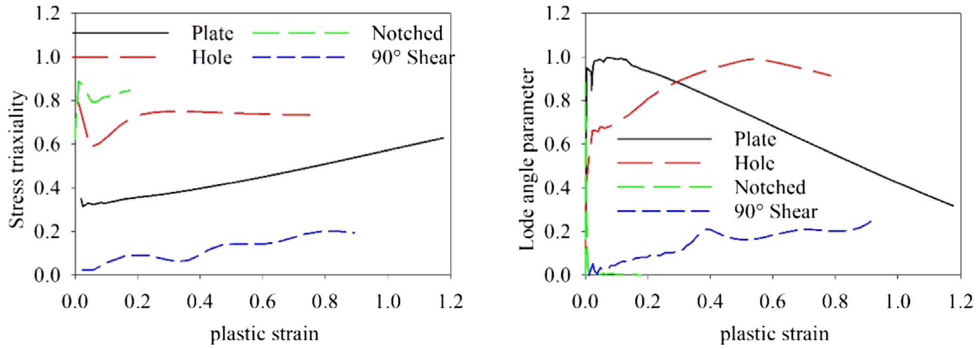

(a) Stress triaxiality η (b) Lode angle parameter $\bar{\theta}$

Fig. 9. Evolution of stress triaxiality and Lode angle parameter in girder flange specimen.

Table 3
Results of coupon tests.

Specimen	Girder flange			Girder web		
	ε_f	η_{avg}	$\bar{\theta}_{avg}$	ε_f	η_{avg}	$\bar{\theta}_{avg}$
Plate	1.1764	0.4567	0.6834	1.1064	0.4329	0.7262
Hole plate	0.7837	0.7229	0.8754	0.6373	0.6773	0.7766
Notched Plate	0.1793	0.8295	0.0162	0.2488	0.8517	0.0145
90° shear Plate	0.9267	0.1228	0.1509	0.6943	0.0853	0.1546

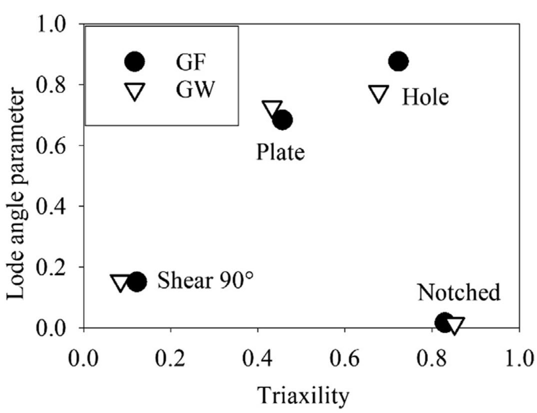

Fig. 10. η_{avg} and $\bar{\theta}_{avg}$ at fracture for different specimens.

Table 4
Calibrated fracture models.

Fracture model	Steel	D_1	D_2	D_3	D_4
Bai model	GF	7.7400	2.8960	1.0710	2.1560
	GW	6.0890	2.8950	0.6550	1.1380
RT1 model	GF	–	–	2.362	1.526
	GW	–	–	2.939	2.257
RT0 model	GF	–	–	1.233	2.324
	GW	–	–	0.778	1.339
CFS model	GF	$D_0 = 1.176$			
	GW	$D_0 = 1.106$			

The forthcoming section also includes this model [Eq. (9)] for comparison purposes.

3.2. Design of the coupon test

The coupon specimens are extracted from the girder web (GW) and girder flange (GF) made from the hot-rolled Q345 H-section beam. The thicknesses of the coupon specimens from these two elements are 5.3 mm (girder web) and 5.8 mm (girder flange), respectively. Table 2 lists a total of five types of coupon specimens, including the plate specimen (No. 1), hole plate specimen (No. 2), notched plate specimen (No. 3), 90° shear plate specimen (No. 4) and 45° shear plate specimen (No. 5). Table 2 also indicates the approximate stress triaxiality and Lode angle parameter for each type of specimens. Fig. 5 shows the geometric configurations and dimensions of the coupon specimens. The calibration of Bai model utilizes four types of specimens (Nos. 1–4 specimens), with different stress triaxiality and Lode angle parameters, to uniquely determine the four parameters in Eq. (7). The calibration of the RT1 and RT0 models makes use of two types of specimens (the Nos. 1 and 2 for RT1 and Nos. 3 and 4 for RT0 model) to estimate the two parameters D_3 and D_4 in Eq. (8). The calibration of the CFS model, on the other hand, uses the No. 1 specimen. The remaining No. 5 specimen is reserved as an independent set to verify the accuracy of the calibrated fracture models.

The loading rate of strain for all tests remains fixed at 0.002/s. The longitudinal deformation of the specimens is measured by an extensometer with a 50 mm gauge length.

3.3. True stress-strain curve

The nominal strain ε_{nom} equals the deformation measured by the extensometer (ΔL) divided by the gauge length of the extensometer (L_0), as indicated in Eq. (10). The nominal stress σ_{nom}, as shown in Eq. (11), is equal to the applied force (F) divided by the initial cross-section area of the specimen (A_0).

$$\varepsilon_{nom} = \frac{\Delta L}{L_0} \tag{10}$$

$$\sigma_{nom} = \frac{F}{A_0} \tag{11}$$

Prior to the specimen necking, the true stress σ and true strain ε derive from the nominal stress σ_{nom} and the nominal strain ε_{nom} by Eqs. (12) and (13),

$$\sigma = \sigma_{nom}(1 + \varepsilon_{nom}) \tag{12}$$

$$\varepsilon = \ln(1 + \varepsilon_{nom}) \tag{13}$$

However, beyond the ultimate stress when necking initiate, plastic deformation localizes in the necking region. Eqs. (12) and (13) become invalid. Instead, the true strain and true stress beyond necking follow the relationship in Eqs. (14) and (15), in which, the applied force F and the cross-sectional area of the necking zone, A, are measured simultaneously,

$$\sigma = \frac{\mathrm{F}}{\mathrm{A}} \tag{14}$$

$$\varepsilon = \ln\left(\frac{\mathrm{A_0}}{\mathrm{A}}\right) \tag{15}$$

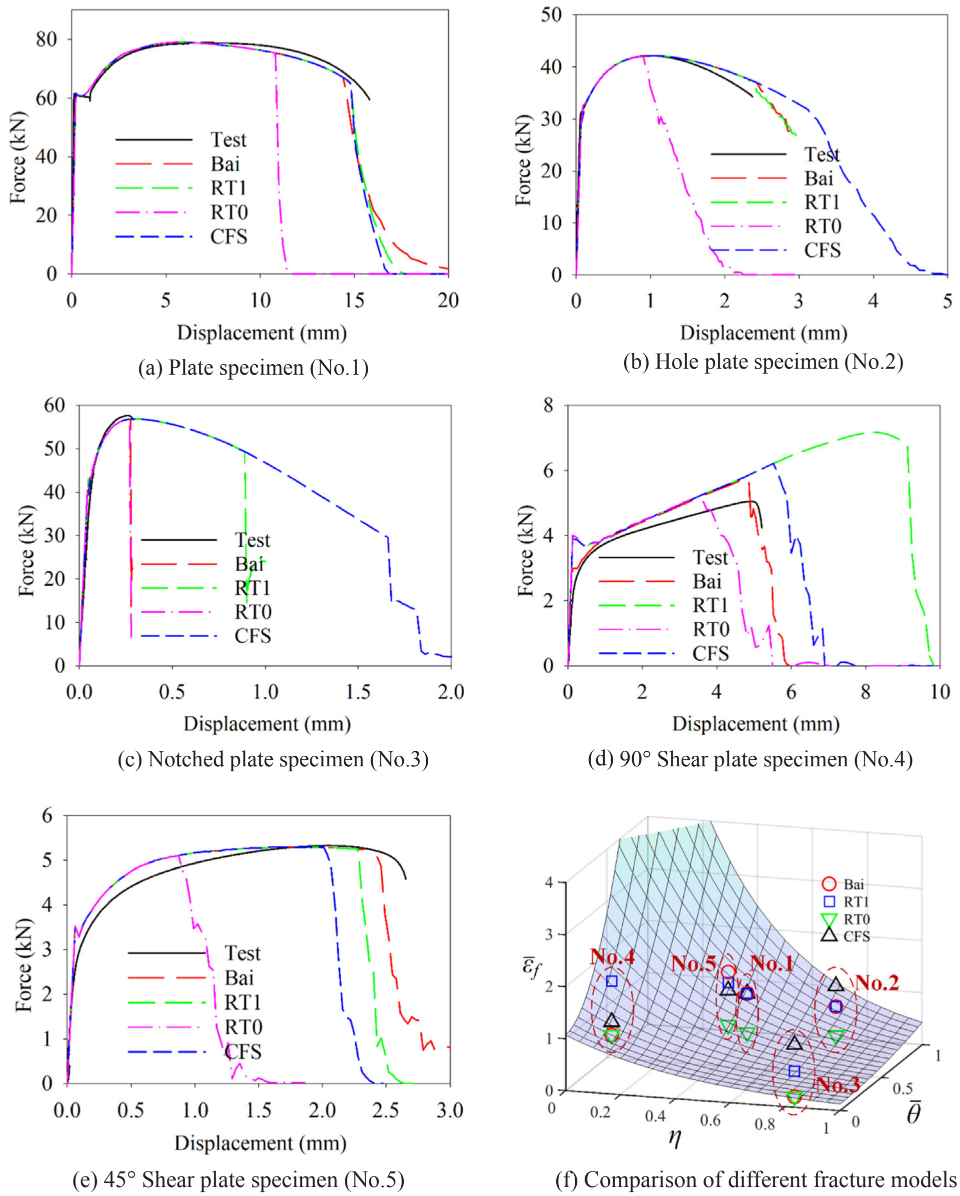

Fig. 11. Comparison of FEM simulation and Test results of the girder flange specimen.

Table 5
Scaling factors by mesh size for Bai model.

Element size (mm)	Scaling factor $i(l_c)$	
	GF	GW
0.5	1	1
1.0	0.775	0.8
1.5	0.625	0.7
2.0	0.505	0.55
3.0	0.33	0.33

As recommended by Jia [23] and Yan [24], the post-necking true stress-strain curve could be assumed as a straight line. This implies that the post necking true stress-true strain relationship requires only a single measurement of A at a discrete post-necking deformation level. Fig. 6 shows the true stress-true strain measured for the girder flange and the girder web. Each of the three elements includes three duplicated flat coupons, which experience the uni-axial tension until fracture occurs. The three duplicated specimens provide an average elongation for each element. The experimental program includes a separate plate

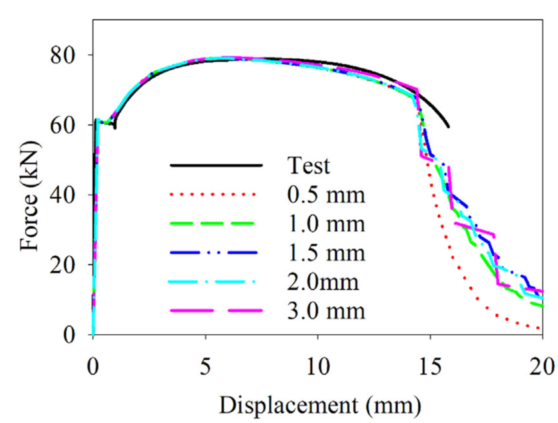

Fig. 12. Comparison force-displacement plots for mesh sizes 0.5 mm, 1.0 mm, 1.5 mm and 3.0 mm.

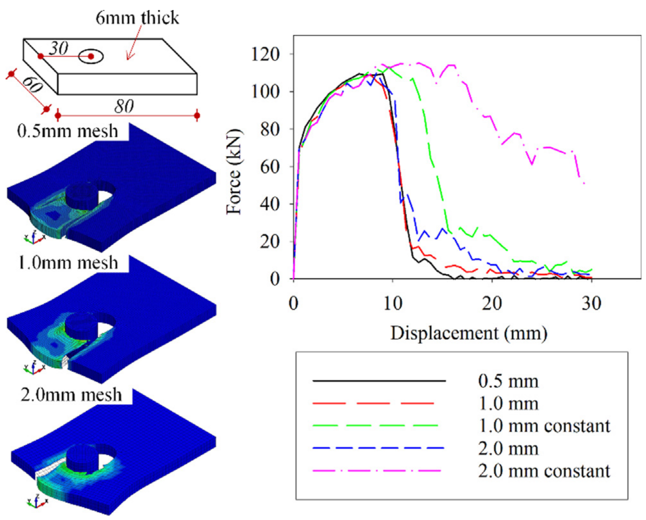

Fig. 13. Comparison force-displacement plots for mesh sizes 0.5 mm, 1.0 mm, and 2.0 mm.

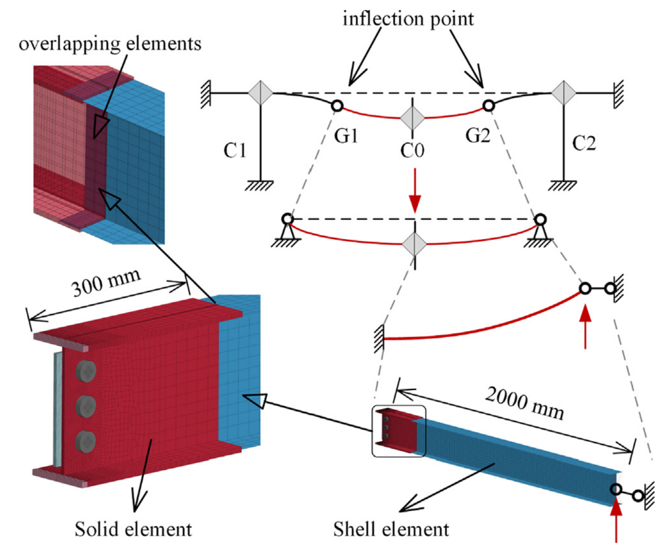

Fig. 15. Girder-to-column connection models.

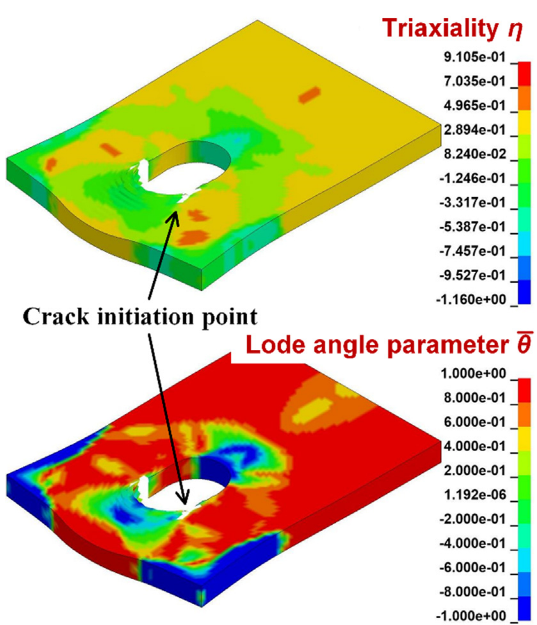

Fig. 14. Triaxiality and Lode angle parameter of the single bolt connection simulation.

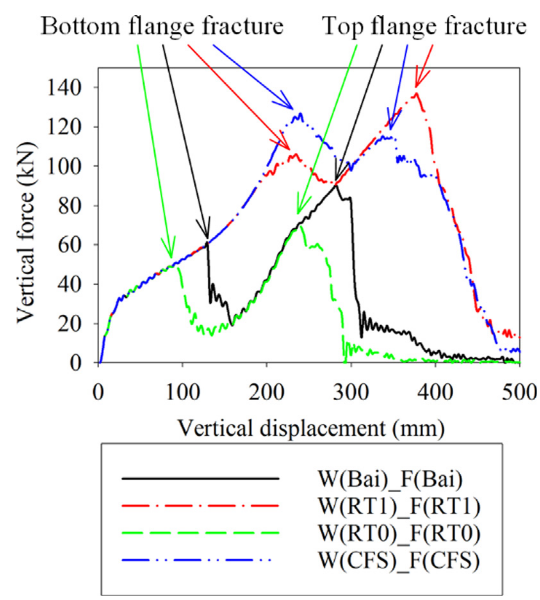

Fig. 16. Load-displacement curves of girder-to-column connection with different fracture locus.

specimen for each element to measure the cross-sectional area beyond necking when the specimen reaches 90% of the average elongation.

3.4. Calibration

The calibration procedure employs the finite element package LS-DYNA R9.1 [25]. The FE model consists of 8-node solid elements with reduced integration, which has one integration point in each solid element. As shown in Fig. 7, the presence of planes of symmetry in the coupon specimens leads to 1/8 models for the Nos. 1–3 specimens, and a 1/2 model for the No. 4 specimen. The element size in the critical region, which anticipates high stresses, equals 0.5 mm, a reliable size recommended by Yan [24]. Fig. 8 shows the comparison of the force-displacement curves between the test and the simulation without fracture modeling. The numerical force-displacement responses agree closely with those measured from the test prior to the fracture failure. The test force-displacement curves represent the average curves among the duplicated specimens for each type of specimen. The relationship between the specimen displacement and the equivalent strain at the critical location (the red element in Fig. 7) derives from the numerical analysis for each case. The center critical elements shown in Fig. 7 corresponds to the mid-thickness position at the center of each specimen. The equivalent plastic strain at fracture ε_f for the center element (shown in Fig. 7) thus equals the equivalent plastic strain corresponding to the displacement at fracture (marked by red circles in Fig. 8).

Fig. 9 illustrates the evolution of the stress triaxiality and Lode angle parameter in the critical element (red element in Fig. 7) up to fracture for the girder flange specimen. The stress triaxiality and Lode angle parameter do not remain constant during the loading procedure. In order to reflect the effect of the loading history, this study calculates the average values of the stress triaxiality and Lode angle parameter, i.e., η_{avg} and $\bar{\theta}_{avg}$, as follows,

$$\eta_{avg} = \frac{\int_0^{\varepsilon_f} \eta d\varepsilon}{\varepsilon_f} \tag{16}$$

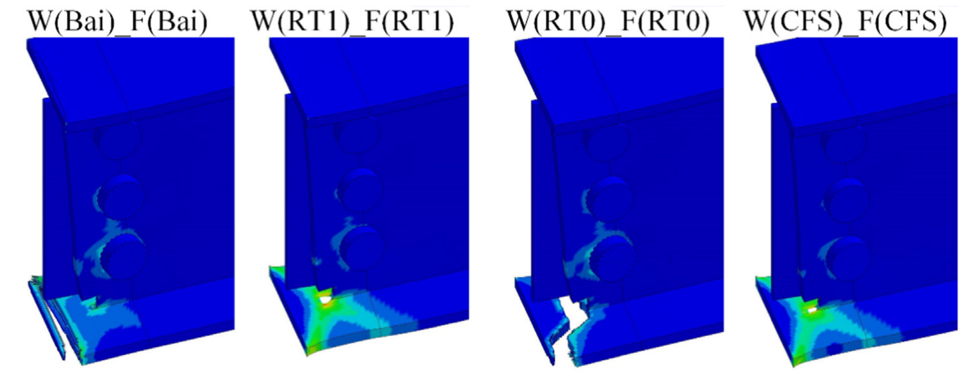

(a) Crack patterns at 200mm

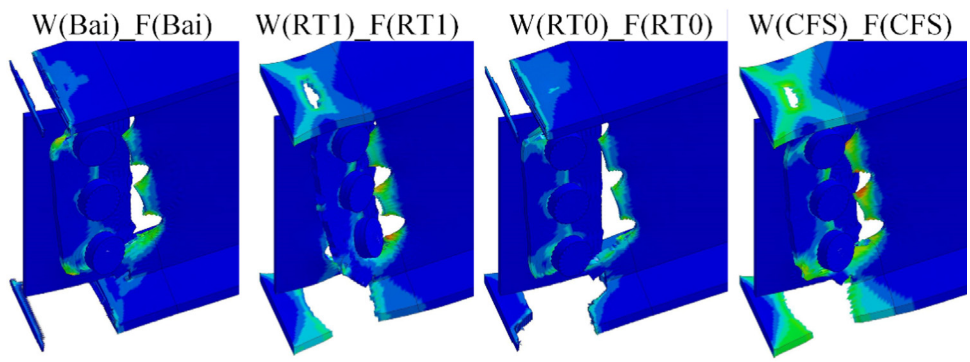

(b) Crack patterns at 400mm

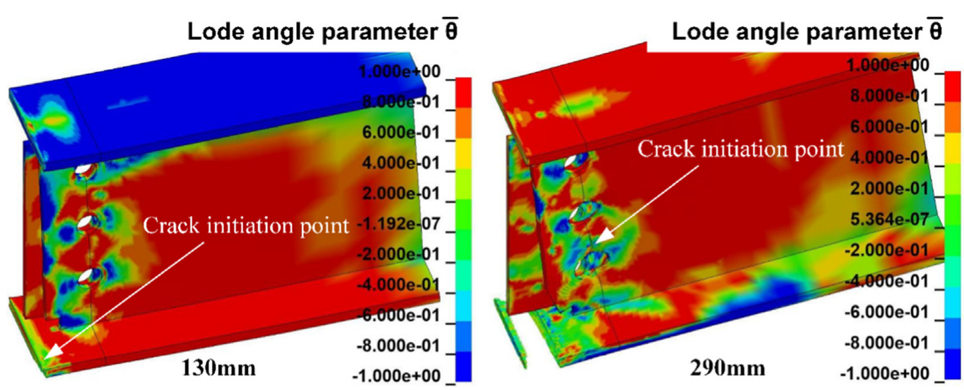

(c) Lode angle parameter distributions in the W(Bai)_F(Bai) case

Fig. 17. Comparison of the failure mechanisms.

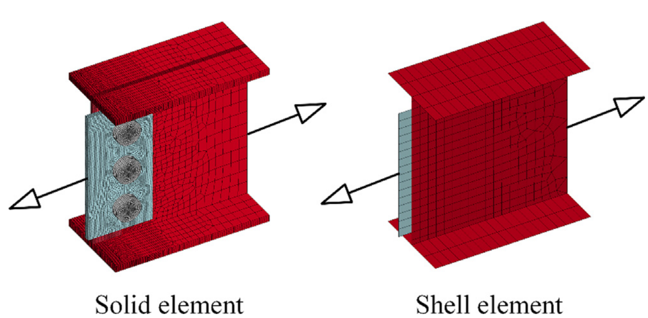

Fig. 18. Bolted shear tab connection models.

$$\bar{\theta}_{avg} = \frac{\int_0^{\varepsilon_f} \bar{\theta} \mathrm{d}\varepsilon}{\varepsilon_f} \tag{17}$$

Table 3 lists a total of four groups of (ε_f, η_{avg}, $\bar{\theta}_{avg}$) values for different types of specimens (Nos. 1–4 specimens). Fig. 10 illustrates the corresponding (η_{avg}, $\bar{\theta}_{avg}$) pairs in η-$\bar{\theta}$ plane. These four types of specimens are located fairly dispersed in the η-$\bar{\theta}$ plane, which facilitates the calibration of the unique fracture locus values. Using the Optimization Toolbox in Matlab, the values of D_1, D_2, D_3, and D_4 can be optimized based on the test data points by Eq. (18), which is chosen to minimize the average error. In Eq. (18), N represents the number of data points used in the fracture locus calibration. Table 4 lists the fracture parameters of the different fracture models.

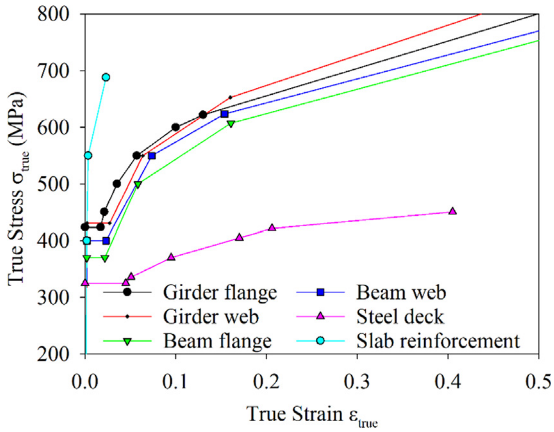

Fig. 19. True stress-strain curves of the shell element.

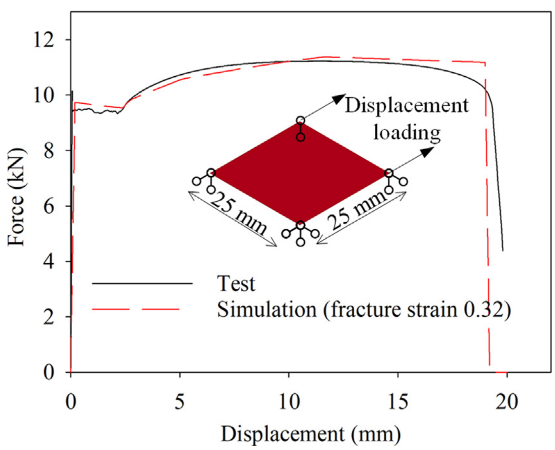

Fig. 20. Comparison of FEM simulation and test result of the steel deck specimen.

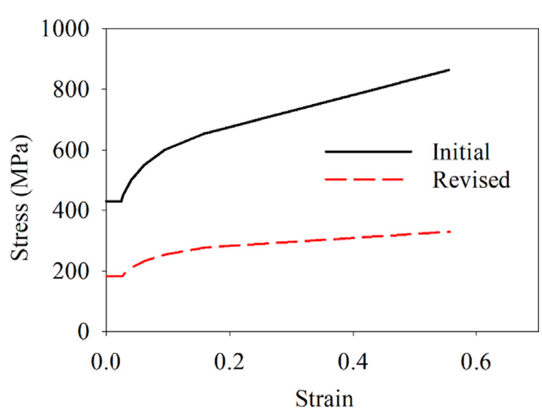

Fig. 21. True stress-strain curve of the shear tab shell element.

$$\mathrm{Min}_{D_1,D_2,D_3,D_4}(\mathrm{Error}) = \mathrm{Min}\left[\frac{1}{N}\sum_{i=1}^{N} |\varepsilon_f(\eta_i, \theta_i) - \varepsilon_{f,i}|\right] \tag{18}$$

Using the fracture locus calibrated above, the finite element simulations reanalyze the coupon specimens by implementing the different fracture models in LS-DYNA, through the No. 224 material in LS-DYNA (Tabulated Johnson-Cook material), which defines the fracture locus by a table of fracture strains corresponding to different stress triaxiality and Lode angle parameter. Fig. 11 compares the force-displacement curves between the coupon test results of the girder flange specimen and the FEM simulations using different fracture models. Fig. 11 also compares the prediction using different fracture models on the 45° shear plate specimen (No. 5). The Bai model predicts closely the initiation of the fracture for all the specimens as reflected in Fig. 11, while the RT1, RT0 and CFS models are only suitable for the specimens used to calibrate them. The fracture strains predicted by these models are illustrated in Fig. 11(f), which is used to explain the deviations of RT1, RT0 and CFS models. The RT0 model is calibrated by Nos. 3 and 4 specimens, for which $\bar{\theta}$ values are close to 0, but the $\bar{\theta}$ values of No. 1, No. 2, and No. 5 specimens are close to 1. Besides, as shown in Fig. 11(f), for the same η, the fracture strain at $\bar{\theta} = 1$ is much higher than that at $\bar{\theta} = 0$. Therefore, for No. 1, No. 2 and No. 5 specimens, the fracture strains predicted by RT0 model are much lower than that predicted by Bai model. Conversely, the RT1 and CFS models, which are calibrated by No. 1 and No. 2 specimens, are more likely to overestimate the fracture strains for No. 3 and No. 4 specimens.

3.5. Mesh-size regularization

The plastic fracture strain in the LS-DYNA's No. 224 material is defined as the product of the functions in Eq. (19).

$$\varepsilon_f = f(\eta, \bar{\theta}) g(\dot{\varepsilon}_p) h(T) i(l_c) \tag{19}$$

where $f(\eta, \bar{\theta})$ is a function of the stress triaxiality η and Lode angle parameter $\bar{\theta}$. In this study, this function follows the fracture models defined in Table 4. $g(\dot{\varepsilon}_p)$, $h(T)$ and $i(l_c)$ are functions of the plastic strain rate $\dot{\varepsilon}_p$, the temperature T and the initial element size l_c, respectively. Even though the progressive collapse of building structures is a dynamic process, the strain rate effect does not affect the structural responses under the specified column removal scenario as noted by Su et al. [26]. Besides, the test is conducted at the room temperature. Therefore, the effect of strain rate and temperature are excluded in this study.

Hence, the final step for the fracture model calibration is to develop the mesh-size scaling function $i(l_c)$ for the element erosion. The mesh-size regularization scaling function $i(l_c)$ defines the plastic failure strain as a function of the element size. The mesh size used in the regularization equals the ratio of the element volume over the area of the largest face of the element. For a perfectly cubical element, the mesh size equals exactly the element side length. The scaling factor derives from numerical simulations of the plate specimen (No. 1) using different mesh sizes, 0.5 mm, 1.0 mm, 1.5 mm and 3.0 mm. Iterative numerical analyses determine the value of the scaling factor by matching the failure displacement in each mesh size with the test measurement. Table 5 lists the scaling factors for the mesh sizes ranging from 0.5 mm to 3 mm. Fig. 12 shows the force-displacement curves for the plate specimens. With the scaling factors, all four simulations with different mesh sizes fail at virtually the same displacement.

Furthermore, a single bolt connection is also simulated with different mesh sizes. The mesh size 0.5 mm is the benchmark case, while the effect of the mesh-size regularization is depicted by comparing the results with or without the mesh-size scaling factor. As shown in Fig. 13, without the scaling factor, the results from the 1.0 mm mesh and 2.0 mm mesh ("1.0 mm constant" and "2.0 mm constant") are not converging. However, the results from the "1.0 mm" and "2.0 mm" mesh size considering the mesh scaling factor predict the fracture evolution successfully. Fig. 14 illustrates the triaxiality η and Lode angle parameter $\bar{\theta}$ distributions in the single bolt connection simulation, and the η and $\bar{\theta}$ at the crack initiation point are approximately equal to 0.1 and 0.2, respectively. The η and $\bar{\theta}$ in this simulation are significantly different from those in the plate specimen as listed in Table 3, which demonstrates that the mesh-size scaling factor remains independent of the triaxiality and Lode angle.

4. Component simulation

This section integrates the material fracture model calibrated in Section 3 in simulating the response of girder-to-column connection,

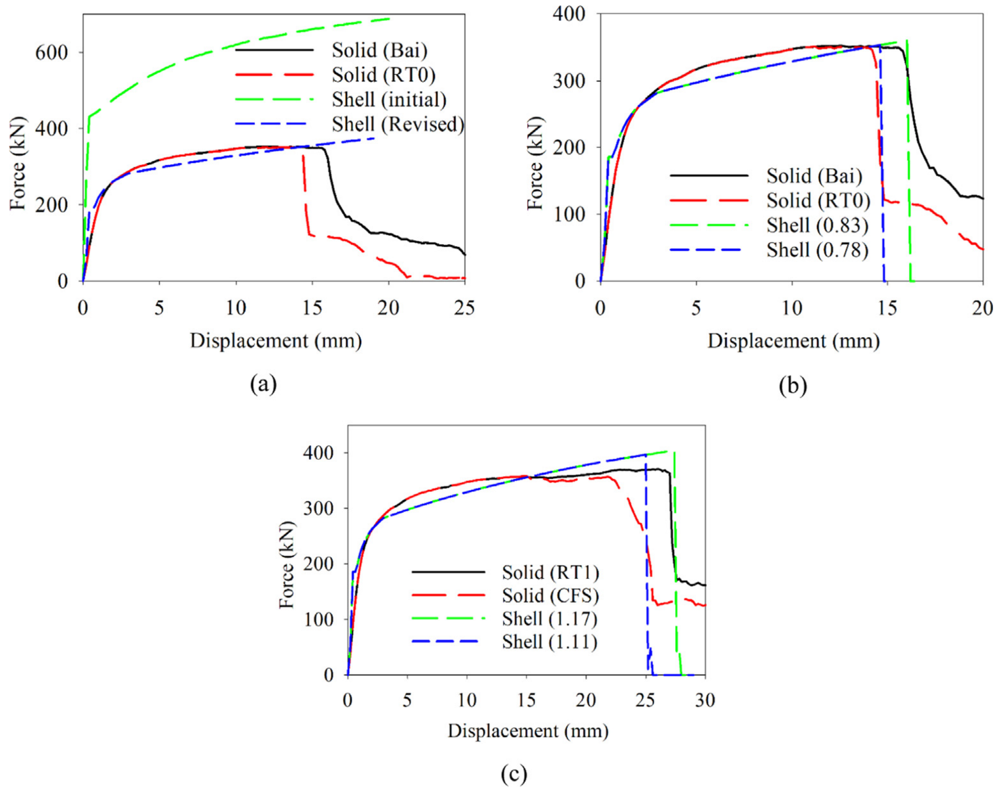

Fig. 22. Bolted shear tab connection simulation.

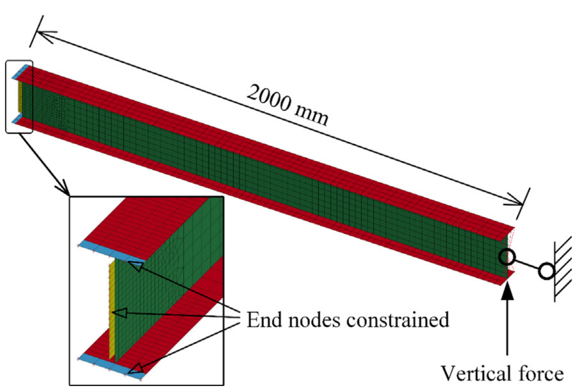

Fig. 23. Girder-to-column connection model.

with the objective to quantify the fracture evolution on the load-deformation responses of the structural components.

4.1. Girder-to-column connection

As shown in Fig. 15, if the composite slab is neglected, the vertical load after the C0 column loss would be only supported by G1 and G2. The girders G1 and G2 are fully restrained at the columns C1 and C2, with an inflection point located approximately at the mid-span of the girder, as illustrated in Fig. 15. Since the column used in this system is relatively strong, the deformation of the column is negligibly small. Given the symmetry property of the system, the FE analysis considers only a girder with a half span, as illustrated in Fig. 15. To enhance the computational efficiency, the FE models remove the columns and simulates the constraints by the columns via constraining corresponding degrees of the freedoms at the ends of the girder flanges and the shear tab. The symmetry condition at C0 leads to the zero horizontal movement with a vertical displacement loading applied at the girder end. Fig. 15 illustrates the mesh details. The girder next to the connection region (300 mm in length) employs solid elements with the smallest size around 1.0 mm–2.0 mm, while the remaining girder uses shell elements to expedite computing speed. The rotational compatibility between solid and shell elements is achieved by overlapping the two types of elements and merging their coincident nodes over a 40-mm length. The contacts in the solid models employ the eroding single surface contact method, which is capable of reestablishing contact after the erosion of elements at the exterior boundary of the model. The steel properties and fracture parameters follow the values validated in Section 3. The shell elements do not include the fracture modeling.

Fig. 16 illustrates the load-displacement curves for the girder-to-column connection using the Bai, RT1, RT0 and CFS models, denoted as W(Bai)_F(Bai), W(RT1)_F(RT1), W(RT0)_F(RT0) and W(CFS)_F(CFS), respectively, where W and F represent girder web and girder flange. Compared with the W(Bai)_F(Bai) case, fracture occurs at a smaller displacement in the W(RT0)_F(RT0) case, while fracture occurs at a larger displacement with a higher resistance for the W(RT1)_F(RT1) and W(CFS)_F(CFS) cases. Besides, the response of W(RT0)_F(RT0) is close to the W(Bai)_F(Bai) case. The two peak loads in Fig. 16 correspond to the fracture of the bottom flange and top flange, respectively. Fig. 17(a) and (b) show the crack patterns at the vertical displacements of 200 mm and 400 mm, respectively. Fig. 17(c) illustrates that the Lode angle parameters computed from the W(Bai)_F(Bai) case at the crack initiation location are close to 0, rather than 1, which explains the similar responses predicted by the RT0 and Bai model. The RT1 and CFS models, in contrast, becomes inaccurate, since they are calibrated using coupon specimens with the Lode angle parameter approximately equal to 1.0. The significant difference between these load-displacement curves in Fig. 16 implies that the choice of the fracture model is vital for the accurate simulation of the girder-to-column connection.

4.2. Bolted shear tab connection

Scaling up of the above Bai model to large-scale structures using solid elements faces significant challenges imposed by the huge

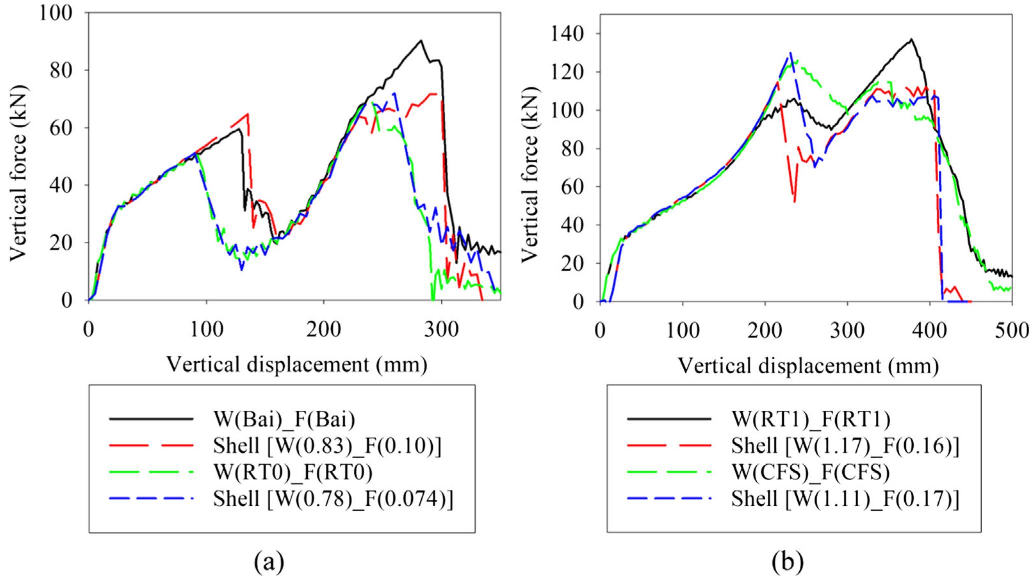

Fig. 24. Simulation results of the girder-to-column connection.

computational cost. The shell element, on the other hand, allows efficient analyses of large-scale engineering structures with reasonable accuracies. This sub-section, therefore, examines the feasibility of shell elements in analyzing the fracture failure in a girder-to-column connection using the properties in the shell element fracture model modified from the solid element fracture model.

Fig. 18 shows the shear tab connection models built from solid elements and shell elements. The shear tab connection experiences axial tension through a displacement controlled loading applied at the end of the girder, with the axial displacement on the shear tab constrained. The steel properties and fracture locus parameters follow the data validated for the solid element model in Section 3. The mesh size in the critical region around the bolt holes of the solid element model is between 1.0 mm and 2.0 mm. The shell element model utilizes a piecewise-linear plasticity model (material 24 in LS-DYNA). The element size of the shell element model is around 10 mm. Fig. 19 shows the true stress-strain curves used in the shell element model. An element erosion procedure removes the elements in the model when the specified failure strain is reached. The fracture strain of the steel deck is determined by a shell element simulation using a 25 mm element, which is 0.32 as shown in Fig. 20.

Firstly, the simulation has been conducted with the true stress-strain relationship in Fig. 19, i.e., the steel property in the shear tab shell element is chosen as the “initial” curve in Fig. 21. As shown in Fig. 22(a), the load-resistance in the shell element model is much higher than the solid element model, as the web cross section has been weakened by the bolt hole. To represent phenomenologically the weakening effect by the bolt hole in shell elements, the true stress-strain curve of the shear tab element has been adjusted for the shell element model. After some iterations, the failure displacement and the resistance of the shell element model are close to that of the solid element model. This adjusted stress-strain curve, which is named as “revised” curve in Fig. 21, will be used in the girder-to-column connection model validation. Fig. 22(b) and (c) shows that the corresponding shell fracture strain of Bai model, RT0 model, RT1 model and CFS model are 0.83, 0.78, 1.17 and 1.11, respectively.

4.3. Shell fracture strain of girder flange element

As shown in Fig. 23, the solid element model in Fig. 15 has been replaced by a shell element model. The ‘revised’ steel property is used in this model, and the load-displacement relationship of this shell element model is illustrated in Fig. 24, in which the shell fracture strain 0.10, 0.074, 0.16 and 0.17 of the flange element can accurately simulate the W(Bai)_F(Bai), W(RT0)_F(RT0), W(RT1)_F(RT1) and W(CFS)_F(CFS) cases, respectively.

4.4. Calibration flow summary

Fig. 24 indicates that the modified shell girder-to-column connection model could accurately reflect the load-displacement relationship derived from the solid element model, for various fracture models used in the solid element model. In general, the accuracy of this shell element model is mainly controlled by three key parameters, the stress-strain curve of the shear tab element, the fracture strains of the flange and shear tab elements. As mentioned above, simulation iterations are necessary to calibrate these three parameters. Therefore, the calibration procedure of the shell girder-to-column connection model is summarized into a flow chart in Fig. 25.

5. Floor system simulation

The floor simulation follows an explicit pushdown method implemented in LS-DYNA R9.1 [25]. In the numerical modeling, as shown in Fig. 26, the girder, beam, column, and steel deck are modeled using 4-node shell elements with reduced integration. The mesh size equals 10 mm and 25 mm in the connection region and other regions. The concrete slab is modeled with 8-node solid elements with reduced integration. The Flanagan-Belytschko stiffness form with an exact volume integration for solid elements [25] is introduced to control the hourglass of the concrete element. The element size of the concrete is also around 25 mm. All the welded steel fabrics are modeled with 2-node truss elements with the element size identical to that of the concrete slab. The shear stud is modeled using 2-node Hughes-Liu beam elements [25] with 2 × 2 Gauss quadrature integration at the cross-section with an element size of 25 mm.

The numerical procedure assumes the perfect bond between the welded steel fabrics and the concrete slab, implemented using the keyword *CONSTRAINED LAGRANGE IN SOLID, and ignores the slip between the two materials. The interaction between the concrete and shear stud follows the same modeling approach.

The interaction between the shear studs and the girder or beam are simulated using nonlinear springs, through a discrete beam element formulation in LS-DYNA (beam element formulation 6) with material

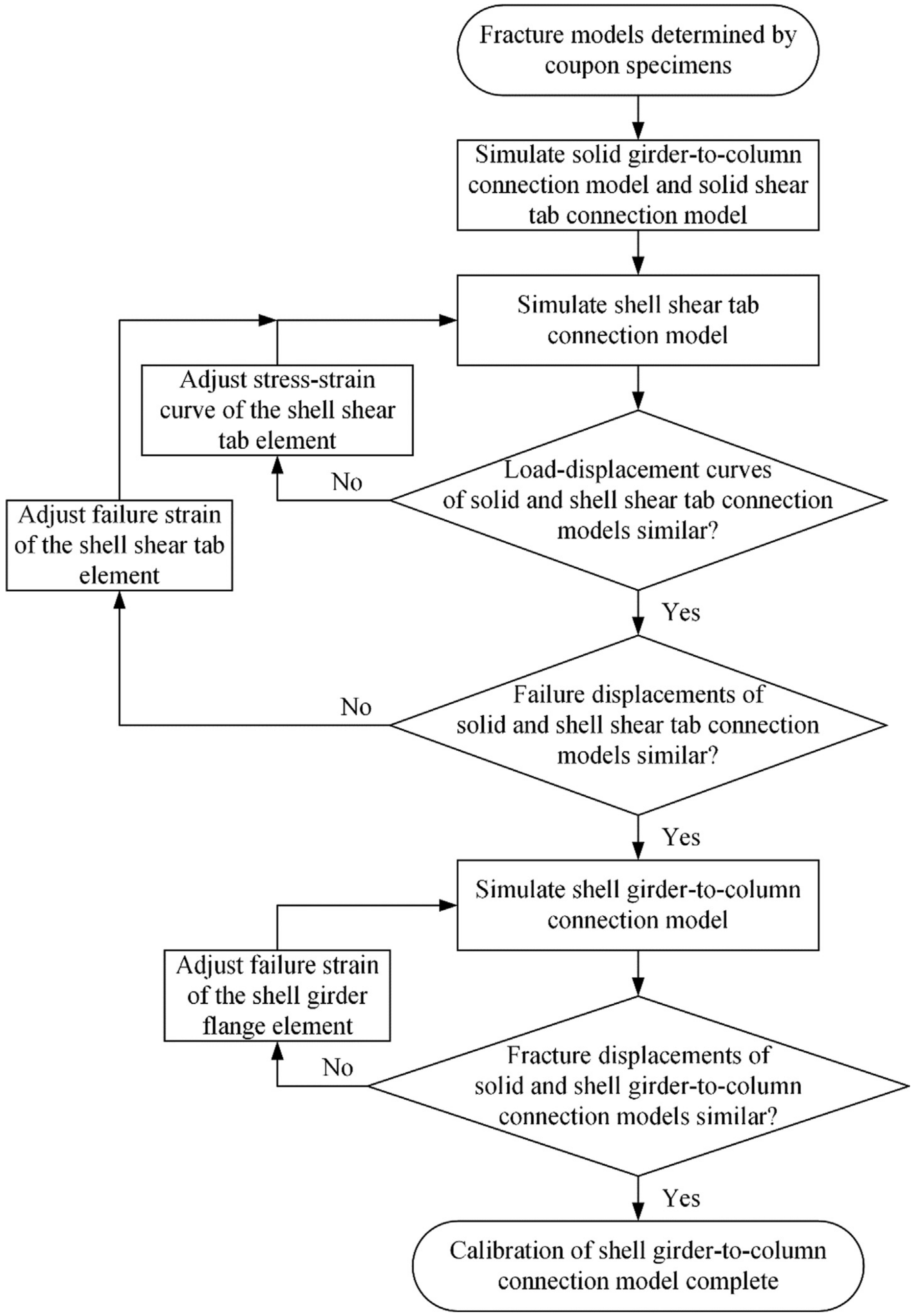

Fig. 25. Calibration flow chart of shell girder-to-column connection model.

model 119. The experimental program includes a separate series of push-out tests to determine the load-displacement input for the nonlinear springs representing the shear stud connection. The load-displacement curves of the shear stud connection along the girder direction and beam direction follow the measured response in Specimen 1 and Specimen 2 shown in Fig. 27(a), respectively. Fig. 27(b) shows the measured load-displacement curves of these push-out tests. As there are four shear studs in the push-out specimen as illustrated in Fig. 27(a), the shear resistance of a single shear stud equals a quarter of the measured resistance in a push-out specimen, as shown in Fig. 27 (c). Also included in Fig. 27(c) are the two piece-wise linear load-deformation curves, which define the load-displacement relationship for the nonlinear spring elements in each of the two shearing directions normal to the longitudinal axis of the shear stud. Each nonlinear spring is deleted when the displacement reaches the maximum slips along either axis. As shown in Fig. 27 (c), the maximum slips of shear stud are defined based on Eurocode 4 [27], which are defined as the load levels reduced to 90% of the peak load. The nonlinear springs have an artificially enlarged stiffness in other four degrees of freedoms to prevent failures in other directions. For the connection between steel members, the tie constraint between each other is formed by sharing the same node. The contact between steel members and concrete slab, and the contact between steel decks and beams are implemented using the automatic surface-to-surface contact with a friction coefficient of 0.5, which is used by Tahmasebinia et al. [28]. As illustrated in Fig. 26, all the degrees of freedoms at the ends of the extended girders, i.e., G7, G8, and extended beams, i.e., B6, B7, B8, are constrained. For the extended girder G5 and G6, the movement along the girder axis is constrained by a spring element, while the movements in other directions are fully constrained. The stiffness of the spring element derives from the

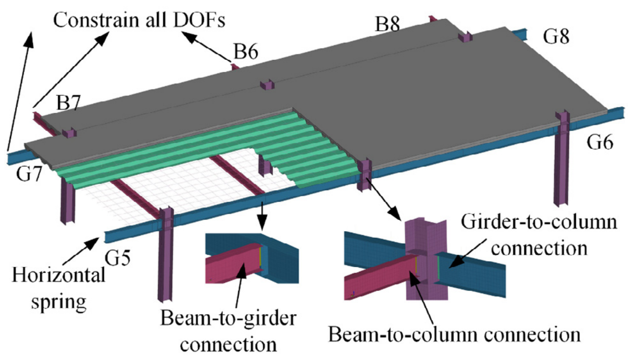

(a) Overall view of the model

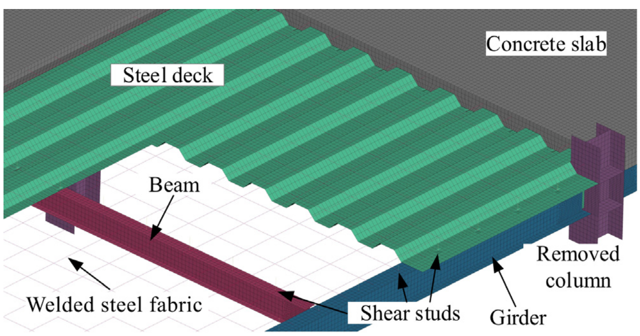

(b) Finite element mesh details

Fig. 26. Finite element model details.

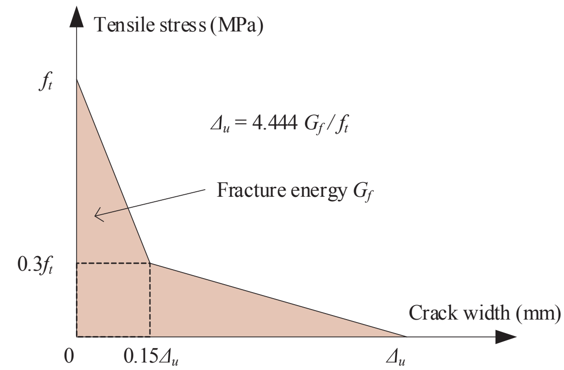

Fig. 28. Uniaxial tensile stress–crack width relationship for concrete.

experimentally measured axial force in G5 and G6 and the corresponding displacements. The axial force of these girders derives from an inverse estimation based on the measured axial strains in G5 and G6, while the axial displacements along the horizontal direction are measured by the Linear Variable Differential Transformer (LVDT) along the horizontal direction. The elastic stiffness of the horizontal spring supports is calculated by dividing the girder axial force by its horizontal displacement equals about 10 kN/mm. The concentrated nodal force is applied to all the nodes of the concrete top surface in the two-bay area to simulate the equally distributed load. The computed resultant vertical force at the column bases is taken as the load carried by the floor system.

The material for the girder, beam and steel deck use the piecewise-linear plasticity model (material 24 in LS-DYNA) defined by the true stress-strain curves in Fig. 19. The shear tab element uses the revised true stress-strain curve in Fig. 21. The welded steel fabrics employ a bilinear elastic-plastic model (material 3 in LS-DYNA), which requires

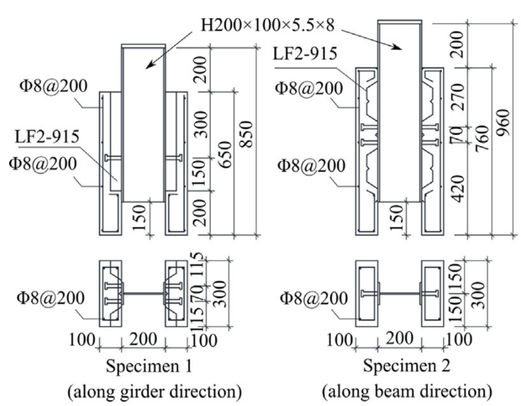

(a) Dimensions of the push-out specimens

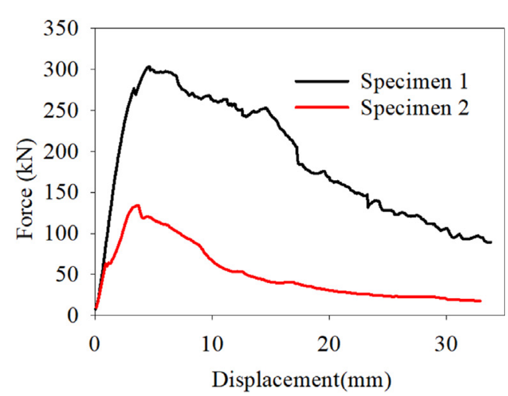

(b) Load-displacement curves

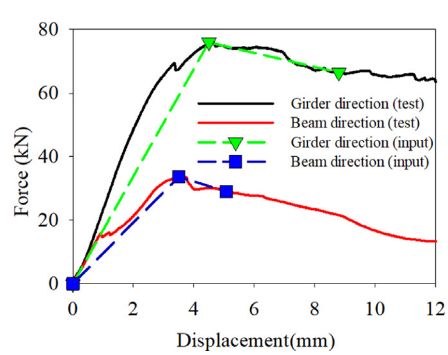

(c) Shear resistance of shear stud

Fig. 27. Push-out specimens.

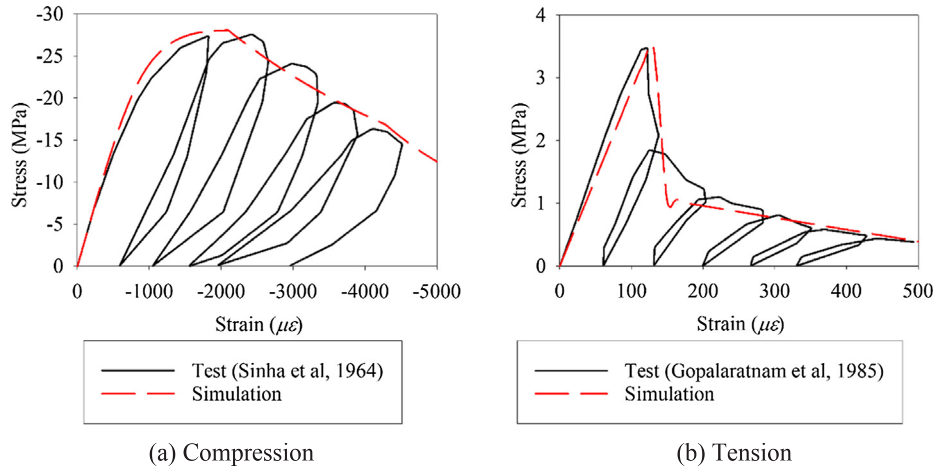

Fig. 29. Compressive and tensile results for concrete.

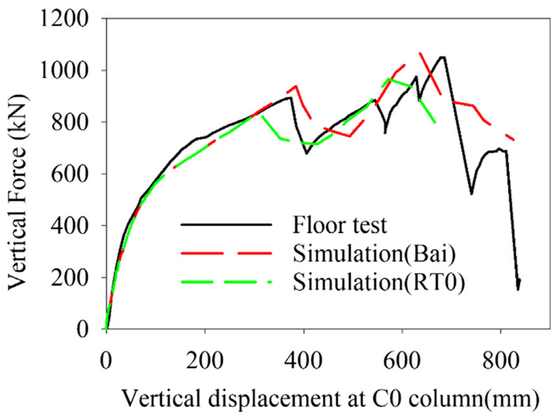

Fig. 30. Simulations calibrated by different fracture model.

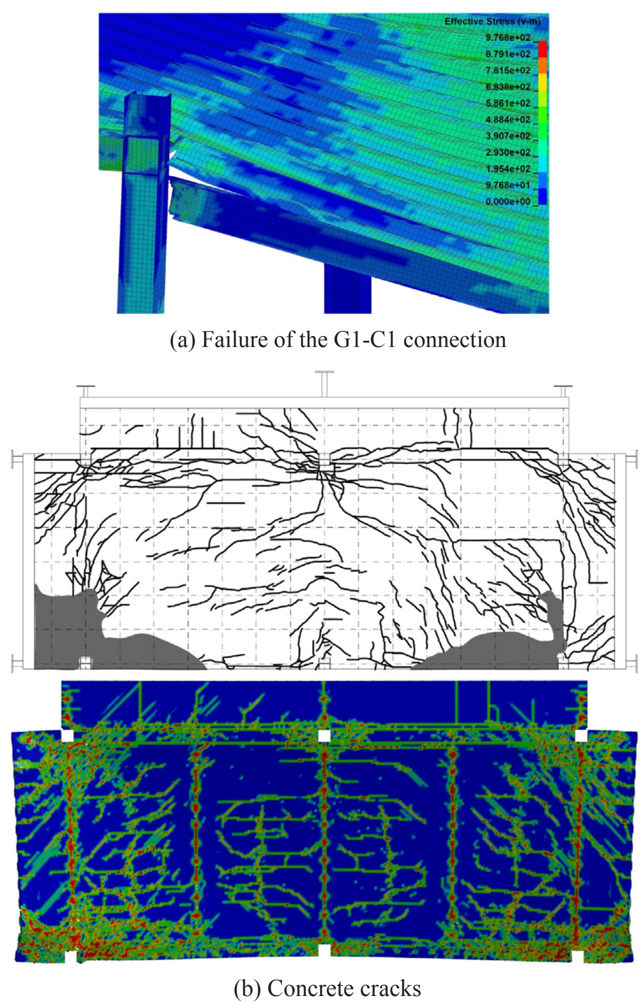

Fig. 31. Failure phenomenon in the simulation calibrated by Bai model.

the input on the elastic modulus, yield strength, tangential modulus after yielding and failure strain. When the strain exceeds the failure strain (equals the elongation in Table 1), the corresponding steel fabric element is to be removed.

A concrete damage plasticity model (CDPM, material 273 in LS-DYNA) is used to simulate the concrete slab, which is based on the works published by Grassl [29,30]. This model is capable of describing the degradation of stiffness, irreversible displacements, the effects of confinement on concrete strength and the realistic response of cyclic loading. Moreover, the tensile and compressive failure simulated by this model is meshed independently. The damage plasticity model follows basically the following equation:

$$\sigma = (1 - \omega_t)\sigma_t + (1 - \omega_c)\sigma_c \tag{20}$$

where σ is the effective stress tensor, σ_t and σ_c are the positive and negative parts of σ, and the scalar ω_t and ω_c are the tensile and compressive damage variables, ranging from 0 (undamaged) to 1 (fully damaged). The brittle behavior of concrete is often characterized by a stress-crack displacement response instead of a stress-strain relationship. In this model, the stress-crack displacement relationship can be defined with different options: linear, bilinear or an exponential tension softening response. This study adopts a bilinear stiffening response as detailed in Fig. 28, where, f_t is the maximum tensile strength, and G_f denotes the fracture energy of concrete that represents the area under the tensile stress-crack displacement curve. The fracture energy G_f depends on the concrete quality and follows Eq. (21) (CEB-FIP Model Code 2010) [31].

$$G_f = 73 f_c^{0.18} \tag{21}$$

where f_c is the compressive strength of concrete. The cubic strength (33 MPa) is converted into the cylindrical strength (26 MPa) based on the CEB-FIP Model Code 2010 [31]. The tensile strength, fracture energy, and elastic modulus are thus equal to 2.65 MPa, 0.131 N/mm, and 29664 MPa, respectively. The other concrete model parameters employ the default value in the CDPM model. Fig. 29 shows the comparison of the numerical and experimental curves [32,33] of concrete using the model variables mentioned above.

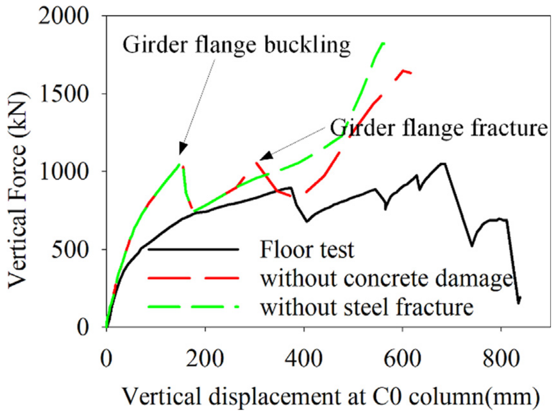

Fig. 32. Comparison of the floor test and simulations without concrete damage and steel fracture models.

Fig. 30 shows that the numerical simulation based on the calibrated Bai model agrees with the experimentally measured load-displacement curve. The essential characteristics of the load-displacement curves, including the ascending, the softening, and the re-ascending stage, are successfully captured. Besides, the failure phenomenon, including the failure of the G1-C1 connection and the concrete cracks on the slab top surface are well captured by the simulation, as shown in Fig. 31(a) and (b). Despite the presence of many reinforcements and shear studs in the concrete slab, the Bai model achieves reasonable accuracy in predicting the load-displacement response and the failure mechanisms at large deformation levels. The RT0 model initiates a fracture failure at a smaller displacement than the Bai model and the test. The numerical analysis also examines the effect of concrete damage and steel fracture. Fig. 32 confirms that both the concrete damage and steel fracture should be considered in the collapse simulation of the composite floor system. The ignorance of either in the numerical simulation leads to an unconservative estimation of the floor resistance with an incorrect failure mode.

6. Conclusions

This paper presents an upscale study to consider the shear fracture material model in the progressive collapse simulation of a steel-concrete composite floor model using macro shell elements. The combined experimental and numerical investigation examines the failures at different engineering scales, which covers: (1) the material failure using five types of coupon specimens with contrast difference in stress triaxiality and Lode angles; (2) the structural component failure in the girder-to-column connection; and (3) the system failure in a full-scale steel-concrete composite floor test. The study presented above leads to the following conclusions:

1. Among the three different fracture models considered, Bai model demonstrates superior performance than the RT model and the CST model, in predicting the initiation and evolution of fracture failure for a wide range of stress triaxiality and Lode angle parameters. The RT model and CST model are limited to the stress triaxiality and Lode angle parameters, from which they are calibrated.
2. Since the fracture models used in this study are strain-based in nature, the numerical implementation of such models exhibit inevitably a mesh size dependence. Nevertheless, the current study proposes a mesh scaling factor for a reasonable range of element sizes anticipated in the engineering simulation using solid elements. The proposed scaling factor leads to similar load-deformation responses for FE models with different element sizes and remains independent of the stress triaxiality and Lode angle experienced by the material.
3. In the moment-resisting connection, the fracture of both the girder flange and girder web depends highly on the Lode angle.
4. To overcome the numerical challenges in simulating large-scale structural systems, this study adopts the macro shell elements to simulate the fracture failure in the steel-concrete composite floor system. The fracture strain in the macro shell elements, in which the Bai model is not directly applicable, derives from an empirical conversion from the corresponding solid elements using the Bai model for different stress triaxiality and Lode angle parameters.
5. In the steel-concrete composite floor system, simulation of both the steel fracture and the concrete damage remains essential to ensure an accurate estimation of the load resistance and the corresponding failure mechanisms.

Declaration of Competing Interest

The authors declare that there are no known conflicts of interest associated with this publication and there has been no significant financial support for this work that could have influenced its outcome.

Acknowledgments

The research presented in this paper was sponsored by the State Key Laboratory of Diaster Reduction in Civil Engineering (Tongji University) through Grant Nos. SLDRCE19-A-03 and SLDRCE16-03 and Natural Science Foundation of China (NSFC) through Grant No. 51378380. Any opinions, findings, conclusions, and recommendations expressed in this paper are those of the authors and do not necessarily reflect the views of the sponsors.

References

[1] Starossek U. Progressive collapse of structures. Thomas Telford, London, UK. 2009.
[2] El-Tawil S, Li H, Kunnath S. Computational simulation of gravity-induced progressive collapse of steel-frame buildings: Current trends and future research needs. J Struct Eng 2013;140(8):A2513001.
[3] Wen H, Mahmoud H. Simulation of block shear fracture in bolted connections. J Constr Steel Res 2017;134:1–16.
[4] Bao Y, Wierzbicki T. On fracture locus in the equivalent strain and stress triaxiality space. Int J Mech Sci 2004;46(1):81–98.
[5] Bao Y, Wierzbicki T. A comparative study on various ductile crack formation criteria. J Eng Mater Technol 2004;126(3):314–24.
[6] Wilkins ML, Streit RD, Reaugh JE. Cumulative-strain-damage model of ductile fracture: simulation and prediction of engineering fracture tests lawrence livermore national lab., CA (USA). San Leandro (CA, USA): Science Applications, Inc.; 1980.
[7] Xue L. Damage accumulation and fracture initiation in uncracked ductile solids subject to triaxial loading. Int J Solids Struct 2007;44(16):5163–81.
[8] Bai Y, Wierzbicki T. A new model of metal plasticity and fracture with pressure and Lode dependence. Int J Plast 2008;24(6):1071–96.
[9] Bai Y. Effect of loading history on necking and fracture. Ph. D. thesis, Massachusetts Institute of Technology. Cambridge; 2007.
[10] Sadek F, El-Tawil S, Lew HS. Robustness of composite floor systems with shear connections: modeling, simulation, and evaluation. J Struct Eng 2008;134(11):1717–25.
[11] Alashker Y, Li H, El-Tawil S. Approximations in progressive collapse modeling. J Struct Eng 2011;137(9):914–24.
[12] Alashker Y, El-Tawil S. A design-oriented model for the collapse resistance of composite floors subjected to column loss. J Constr Steel Res 2011;67(1):84–92.
[13] Alashker Y, El-Tawil S, Sadek F. Progressive collapse resistance of steel-concrete composite floors. J Struct Eng 2010;136(10):1187–96.
[14] Li H. Modeling Behavior and design of collapse-resistant steel frame buildings. MI: Ann Arbor; 2013.
[15] Main JA, Liu J. Robustness of prototype steel frame buildings against column loss: assessment and comparisons. Structures congress 2013: bridging your passion with your profession; 2013; 43–54.
[16] Fu F. Progressive collapse analysis of high-rise building with 3-D finite element modeling method. J Constr Steel Res 2009;65(6):1269–78.
[17] Fu F. 3-D nonlinear dynamic progressive collapse analysis of multi-storey steel composite frame buildings-Parametric study. Eng Struct 2010;32(12):3974–80.
[18] Kwasniewski L. Nonlinear dynamic simulations of progressive collapse for a multistory building. Eng Struct 2010;32(5):1223–35.
[19] Standardization Administration (SAC) of the People's Republic of China. (2010). Hot-rolled H and Cut T section steel. GB/T11263-2010; 2010.
[20] Wierzbicki T, Xue L. On the effect of the third invariant of the stress deviator on ductile fracture. Impact and Crashworthiness Laboratory. Technical Report; 2005; 136.

[21] Wen H, Mahmoud H. New model for ductile fracture of metal alloys. I: Monotonic loading. J Eng Mech 2015;142(2):04015088.
[22] Rice JR, Tracey DM. On the ductile enlargement of voids in triaxial stress fields. J Mech Phys Solids 1969;17(3):201–17.
[23] Jia LJ, Kuwamura H. Ductile fracture simulation of structural steels under monotonic tension. J Struct Eng 2013;140(5):04013115.
[24] Yan S, Zhao X, Wu A. Ductile fracture simulation of constructional steels based on yield-to-fracture stress–strain relationship and micromechanism-based fracture criterion. J Struct Eng 2018;144(3):04018004.
[25] Ls-Dyna L. Keyword user's manual. Livermore Software Technology Corporation; 2016. p. R9.1.
[26] Su Y, Tian Y, Song X. Progressive collapse resistance of axially-restrained frame beams. ACI Struct J 2009:106(5).
[27] Eurocode 4. Design of composite steel and concrete structures, part 1-1: general rules and rules for buildings (ENV 1994-1-1). CEN; 2004.
[28] Tahmasebinia F, Ranzi G, Zona A. A probabilistic three-dimensional finite element study on simply-supported composite floor beams. Aust J Struct Eng 2011;12(3):251–62.
[29] Grassl P, Jirásek M. Damage-plastic model for concrete failure. Int J Solids Struct 2006;43(22–23):7166–96.
[30] Grassl P, Xenos D, Nyström U, et al. CDPM2: a damage-plasticity approach to modelling the failure of concrete. Int J Solids Struct 2013;50(24):3805–16.
[31] Comité euro-international du béton. CEB-FIP model code 2010: design code. Telford; 2012.
[32] Sinha BP, Gerstle KH, Tulin LG. Stress-strain relations for concrete under cyclic loading. ACI J 1964;61(2):195–212.
[33] Gopalaratnam VS, Shah SP. Softening response of plain concrete in direct tension. ACI J 1985;82(3):310–23.